A facile route to the synthesis of carbon replicas cast from narrow-mesoporous matrices

Rafał Janus [a,*], Sebastian Jarczewski [b], Jacek Jagiello [a], Piotr Natkański [b], Mariusz Wądrzyk [a], Marek Lewandowski [a], Marek Michalik [c], Piotr Kuśtrowski [b]

[a] *AGH University of Krakow, Faculty of Energy and Fuels, al. A. Mickiewicza 30, 30-059, Kraków, Poland*
[b] *Jagiellonian University, Faculty of Chemistry, ul. Gronostajowa 2, 30-387, Kraków, Poland*
[c] *Jagiellonian University, Institute of Geological Sciences, ul. Gronostajowa 3a, 30-387, Kraków, Poland*

ARTICLE INFO

ABSTRACT

Carbon replicas find a variety of applications in chemical sciences and even in medicine. However, tedious synthesis hinders their application to the laboratory scale hitherto. Here, we develop a facile procedure for the synthesis of CMK-1 and CMK-2 materials cast from narrow-mesoporous hard templates, i.e. MCM-48 and SBA-1, respectively. The proposed recipe is reproducible, operates under mild conditions using basic laboratory equipment and a renewable carbon source (furfuryl alcohol). It relies on the solvent-polarity-controlled deposition of a polar carbon precursor on unmodified silica in a non-polar medium. Such a self-regulating process provides even coverage of the matrix with polymer leading to the formation of carbon mesostructures of exquisite replication fidelity and structural homogeneity while maintaining the primary morphology. The in-depth study of physisorption data employing the dual gas model (simultaneous N_2 and CO_2 fitting) disclosed the mixed, micro-mesoporous nature of the materials. This tool was found to provide a fair, comprehensive textural characterization, especially useful for materials with pore sizes on the boundary between micro- and mesopores. Therefore, this research paves the way for the manufacturing and application of CMK-1 and CMK-2 carbon replicas on a larger scale. Additionally, it provides certain hints for the robust textural characterization of such materials.

1. Introduction

According to the aphorism attributed to Aristotle, 'nature abhors a vacuum'. Indeed, it is generally known that the formation of close-packed bodies is thermodynamically favorable. Nevertheless, porous materials are actually more interesting from the point of view of both pure and applied science due to their specific properties.

Although man has been aware of the specificity of porous materials since antiquity, just in the 18th century, the world saw a surge in the field (discovery of zeolites, first research on gas adsorption on charcoal [1]). In the early 20th century, coal porosity and its methane-capturing capability were extensively studied [2]. Recent decades have brought tremendous progress in the tailored synthesis strategies that allow receiving advanced porous materials of various deliberately programmed functionalities, often truly creative [3–6].

Even a cursory consideration of the properties of nanoporous bodies is thought-provoking. For example, a simple calculation discloses that the cumulative length of the pores contained in 1 g of a typical mesoporous solid with an apparent surface area of 1000 m^2 g^{-1} and cylindrical, 5 nm wide channels (e.g. MCM-41 or SBA-15), virtually equals $6.4 \cdot 10^7$ km, which is about half the average Earth-Sun distance. Furthermore, 1 g of a typical activated carbon contains about 10^{20} adsorption sites [2] (meanwhile, the number of stars in the Milky Way is estimated to be 10^{11}). In recent years, scientists outdo each other in the synthesis of materials with an ultrahigh, say, 'void content', and extremely developed specific surface area, therefore being macroscopically ultralight [7]. Suffice to refer to the reports on an ultra-flyweight carbon aerogel with a bulk density of 0.00016 g cm^{-3} [8], and a mesoporous metal-organic framework with an apparent surface area of 7800 m^2 g^{-1} [9].

Among the immensity of porous materials, the family of ordered mesoporous carbons (OMCs) occupies a prominent place. OMCs, alternatively termed *carbon replicas*, have enjoyed unflagging interest from the scientific community since 1999, when the pioneering synthesis of

porous carbon with structural periodicity called CMK-1 was reported [10]. This is not surprising given the unique properties of OMCs. First, although replicas are atomically disordered, they exhibit the long-range ordering of pore system [10–14]. Second, their textural parameters, structural array and surface composition can be intentionally tailored either already at the synthesis stage or by given *ex post* modifications [12,14–16]. Third, OMCs show low bulk densities and good thermal and electrical properties [12,14,17–20]. Fourth, the surfaces of replicas are inherently hydrophobic, and their chemical inertness exceeds that of silicas and aluminosilicates [12,21,22]. Fifth, the mechanical rigidity of OMCs also outperforms mesoporous silicas [12,17–20,23]. Finally, it should be mentioned that depending on the purpose, one may choose between porous material of polar (silicas, aluminosilicates, etc.) or nonpolar character (carbon replicas), characterized by similar textural parameters (particularly pore size), though. This creates excellent opportunities for designing, say, *tailor-made* functional materials, especially for adsorption and separation applications [24–27].

Certainly, these properties have borne fruits in many attempts to apply OMCs as versatile functional materials for various practical purposes, such as adsorption and catalysis [16,28–35], hydrogen storage and CO_2 capture [36–38], and electrochemical engineering [39–41]. Moreover, the excellent biocompatibility of OMCs paved the way for their use in controllable intracorporeal drug delivery [42,43] and extracorporeal blood purification (dialysis) [44]. Carbon replicas also pose a convenient testing ground for research on the fundamental phenomena occurring within nanoconfined spaces, where the dispersion forces come into play. In this context, modeling of diffusion and host-guest interaction was being studied [45,46]. For example, a curious effect of contraction-relaxation of the OMC framework along with the adsorption-desorption cycle has recently been reported [47]. Interesting research has also been published dealing with the confrontation of theoretical simulation vs. experimental data of structural and textural properties of carbon mesostructures [48–50]. It was empirically evidenced that the nanoconfinement effects in porous carbons can affect the kinetics of certain molecular-scale processes. A spectacular example can be the synthesis of methane clathrates within the structure of porous carbon, where their formation proceeds faster and under milder conditions than those in natural deep-sea sediments [51].

Though, challenging synthesis routes have been a barrier that limited the manufacturing and application of OMCs on a larger scale. The recipes reported so far are mostly multistep (e.g. required initial modification of the silica surface, e.g. Al^{3+} incorporation, or multiple impregnation of the matrix with a carbon precursor), which makes them laborious and energy-consuming. Some of these need the use of advanced apparatus (e.g. CVD) and severe conditions (e.g. vacuum carbonization). In general, two synthetic approaches are employed, namely *soft-* and *hard templating* [52,53], the latter is mostly exploited as technically easier; besides, it allows for obtaining materials of better structural quality.

In our recent work, we proposed a facile variant of the *hard templating* route universal for the synthesis of both *hollow-* and *rod-type* structures [54]. The concept relies on a solvent polarity-controlled deposition of carbon source (poly(furfuryl alcohol)) in silica suspended in a non-polar liquid medium (toluene). The favored adsorption of the polar monomer on the free silanols provides even coverage of the matrix with polymer [54,55]. Following this procedure, we obtained six high-quality CMK-*n* structures (*n* = 3, 5–9) cast from three silicas with relatively broad mesopores of 7.5–8.5 nm (i.e. SBA-15, SBA-16, and KIT-6) [54].

It is intelligible that the difficulty of uniform incorporation of carbon precursor within a channel system of mineral template increases with a decrease in its pore diameter [10,33,54]. Additionally, the complexity of the pore's shape also comes into play. This was an incentive to investigate the applicability of our procedure for nanoreplication of narrow-mesoporous silicas with a complex tortuosity of pore systems, such as MCM-48 and SBA-1 (both of a 3D cubic array and the pore size of about 3.5 nm). The nanoreplication of the former leads to the formation

of two carbon mesostructures called CMK-1 and CMK-4. The CMK-1 replica features lower spatial symmetry than mother silica (i.e. it transforms from $Ia\overline{3}d$ distinctive of MCM-48 towards $I4_132$ for the ultimate carbon [12,22,56], viz. Scheme 1). This stems from the spontaneous displacement of the two interwoven (albeit independent) enantiomeric carbon sub-frameworks upon mineral matrix removal. Meanwhile, the CMK-4 replica shares common symmetry with the parent silica. Interestingly, the factors governing whether CMK-1 or CMK-4 is obtained, have not been unraveled [12,56]. The same applies to the CMK-2 carbon, an exact negative structure of SBA-1, which has also been rarely studied despite its interesting array ($Pm\overline{3}n$); Scheme 1 [10,12,18,23,57].

In this study, we put efforts to synthesize the CMK-1 and CMK-2 structures by adopting our recently reported method (CMK-4 synthesis will be the case for a separate article) [54]. It was proven that readily modification of our procedure extends its applicability also for the nanoreplication of silica matrices possessing narrow mesopores.

A comprehensive investigation of structural and textural characteristics (XRD and physisorption), as well as morphology and phase purity of the carbons (SEM, TEM, TG) disclosed excellent replication fidelity and a long-range ordering of the replicas surpassing in quality-wise the majority of suchlike materials that have been reported thus far. Both synthesized carbons reveal a mixed micro-mesoporous character of their carbonaceous matter itself, similar to the *rod-type* structures reported recently [54]. Furthermore, it was found that the dual gas model (combined N_2 and CO_2 fitting [58–60]) tool offers an exhaustive textural characterization. It allows for calculating the pore size distributions rectified from artifacts commonly found on the boundary between micro- and mesopores. This is of paramount importance for the reliable characterization of materials such as CMK-1 and CMK-2.

## 2. Experimental section

2.1. Materials

All chemicals were commercially available and used as received. Tetraethyl orthosilicate (TEOS, 98.0 %) was supplied by Acros Organics, PEO–PPO–PEO triblock copolymer (Pluronic P123, $\overline{M}_w \approx 5800$ g mol^{-1}), hexadecyltrimethylammonium bromide (CTAB, ≥96.0 %), and furfuryl alcohol (FA, 98 %) were purchased from Sigma-Aldrich, hydrofluoric acid (48 %, pure p.a.) was supplied by Merck, hydrochloric acid (35–38 %, pure p.a.), ammonia water (25 %, pure p.a.), tartaric acid (TA, pure p.a.), toluene (pure p.a.), ethanol (96 %, pure p.a.), isopropanol (≥99.5 %), and anhydrous sodium sulphate (99.0 %) were purchased from Avantor Performance Materials Poland.

2.1.1. MCM-48 and SBA-1

Mesoporous MCM-48 and SBA-1 silicas were synthesized following the methods reported elsewhere [61,62] using the molar gel compositions as shown in Table S1. The detailed synthesis procedures are provided in *Supplementary Information*. The calcined MCM-48 and SBA-1 matrices hereafter are marked as M48 and S1, respectively. Additionally, small amounts of the as-made materials were calcined under a static air atmosphere using the same thermal regime as for the carbonization of poly(furfuryl alcohol)/silica composites (850 °C for 4 h with a heating rate of 1 °C min^{-1}). These counterparts were labeled as M48@850 and S1@850.

2.1.2. Carbon replicas

Two carbon replicas were synthesized from the S1 and M48 matrices according to a slightly modified procedure of the surface-selective precipitation polycondensation of furfuryl alcohol on the hard template in its toluene suspension, as reported in our recent papers [54,55]. The CMK-1 material was cast from M48, while the CMK-2 replica was derived from the S1 template, as shown in Table 1. The polymer/SiO_2
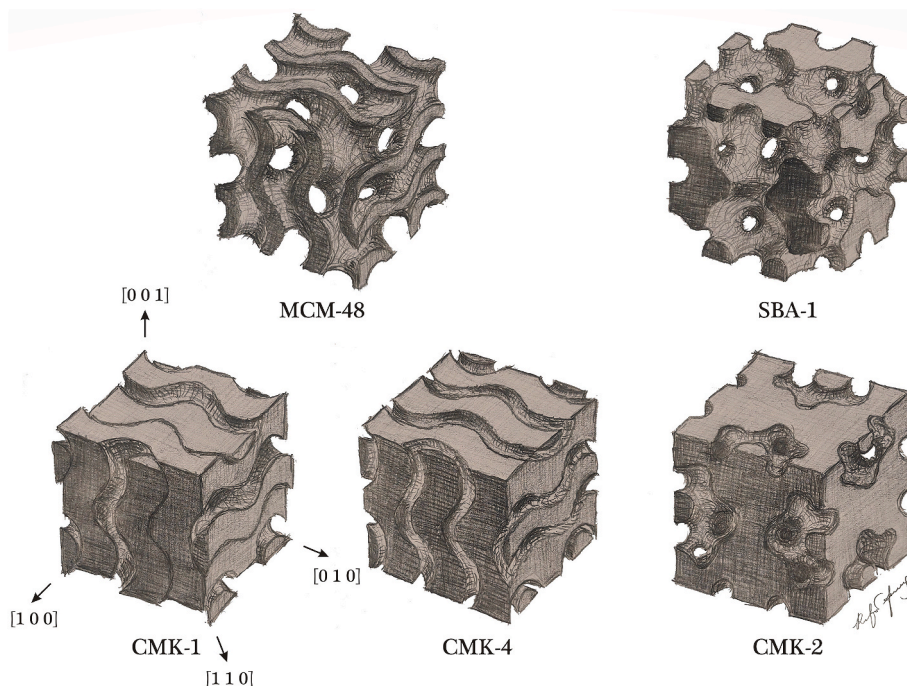
Scheme 1. Pictorial sketch of the parent silica matrices (top) and their negative carbon daughter structures (bottom). In the case of CMK-1, the sub-frameworks displacement occurs diagonally to the unit cell contour (i.e. along the [1 1 0] direction) [22,56].

Table 1
Intended loading of silica matrices with carbon precursor providing the formation of the desired carbon replicas.

Silica matrix (space group)	Intended PFA/SiO$_2$ mass ratio	Carbon replica	
		Structure	Space group
M48 ($Ia\bar{3}d$)	3.8	CMK-1	$I4_1 32$
S1 ($Pm\bar{3}n$)	2.2	CMK-2	$Pm\bar{3}n$

ratios were individually optimized beforehand toward obtaining the target carbon structures. The optimal polymer loadings were those that guaranteed the highest possible XRD intensity accompanied by the narrowest peaks, and the highest textural parameters (specific surface area and total pore volume).

The incorporation of the carbon precursor (poly(furfuryl alcohol), PFA) into the silica pore system was carried out in a 100 cm^3 round-bottom flask sealed with a reflux condenser and immersed in an oil bath placed on a magnetic stirrer. Amount of 0.80 g of freshly calcined silica was added at room temperature (20 °C) under vigorous stirring (850 rpm) to a mixture containing toluene, anhydrous sodium sulphate, furfuryl alcohol, and tartaric acid (note: the use of a freshly calcined matrix and a fresh monomer is of decisive importance). The intentional PFA/SiO$_2$ mass ratios given in Table 1 were adjusted by the mass of FA used. The total mass of toluene and monomer was kept constant at 27.00 g. Also, the TA/FA, and Na$_2$SO$_4$/FA mole ratios were fixed at 0.50 and 0.15, respectively. After immersion of the silica matrix in the reaction system and vigorous stirring (850 rpm) at room temperature for 1 h, the suspension was started to heat up to 100 °C with a heating ramp of 2 °C min^{-1} (this is the modification of the original recipe; the extended contact time of the monomer with the silica surface at room temperature and a slow temperature increase enable the monomer molecules to diffuse through the entire porous structure of the silica). Since reached the desired temperature, the mixture was isothermally held for the next 24 h, constantly stirring (850 rpm). The resulting PFA/SiO$_2$ composite was then separated on a Büchner funnel, washed with 30 cm^3 of toluene, and dried at 105 °C overnight. Eventually, TA and Na$_2$SO$_4$ were rinsed

from the composite by washing with hot distilled water with a few drops of ethanol (added to enhance the wettability of the composite) and dried again at 105 °C for 48 h.

The composites, labeled as PFA–*Y*–x (*Y* means the hard template and x refers to the intended PFA/SiO$_2$ mass ratio), were carbonized in a tunnel quartz furnace under an argon atmosphere (40 cm^3 min^{-1}) at 850 °C for 4 h with a heating rate of 1 °C min^{-1}. Finally, the silica matrix was etched by double treatment with 10 wt% HF at room temperature for 90 min (30.0 cm^3 of HF per 1.00 g of carbonizate), washed with distilled water and acetone, and dried at 105 °C. The carbonizates were labeled as C–*Y*–x, while the corresponding CMK-*n* replicas were marked according to the generally adopted notation (Table 1) [12].

2.2. Methods

Textural parameters of the materials were investigated by means of conventional gas physisorption technique working in a volumetric mode. Low-temperature (−196 °C) adsorption-desorption of nitrogen isotherms were recorded for all samples. Additionally, for the carbon replicas, the CO$_2$ adsorption isotherms at 0 °C were collected at $p/p_0 < 3 \cdot 10^{-2}$. The measurements were carried out using an ASAP 2020 sorptometer (Micromeritics), previously outgassing the samples at 250 °C (silicas, carbonizates, and ultimate replicas), and 50 °C (PFA/SiO$_2$ composites) for 6 h under vacuum. The relevant calculation details can be found in *Supplementary Information* and in previous works [15,34,54,55,63–66].

Structural parameters were determined by means of low-angle X-ray powder diffraction (XRD) using a D2 Phaser instrument (Bruker) equipped with a LYNXEYE detector. XRD patterns were acquired with Cu Kα radiation ($\lambda = 1.54184$ Å) in the angular ranges of $2\theta = 1.00$–$7.00°$ and 10.00–$60.00°$ (for replicas) with an interval of $0.02°$. The resulting patterns (viz. Fig. 3.) were normalized to the intensity of the dominant reflections, i.e. (2 1 1) for M48 and its relatives, and (2 1 0) for S1 and related materials.

Transmission electron microscopy (TEM) imaging was performed using a FEI Tecnai TF20 X-Twin (FEG) apparatus operated at 200 kV. The specimens were prepared by the dispersion of the powder samples in

isopropanol followed by sonication for 10 min and deposition onto carbon-coated copper grids using the drop-casting technique.

Scanning electron microscope (SEM) images were recorded using a Hitachi S-4700 field emission apparatus (FE-SEM) working at 20 kV. The samples were placed on carbon adhesive discs and coated with gold.

High-resolution thermogravimetric analyzes (TG) were performed using a SDT Q600 analyzer (TA Instruments). Amount of ca. 10 mg of a sample was placed in a corundum cup and then heated from 30 to 1000 °C under an air atmosphere (100 cm^3 min^{-1}). The heating rate of 20 °C min^{-1} was applied for the investigation of the real amounts of polymer deposited on the silica, while for the thermo-oxidative stability study of the carbon replicas the ramp of 5 °C min^{-1} was set (for details refer to *Supplementary Information*) [54].

Elemental analysis (EA) measurements were carried out using an EA3100 (EuroVector) analyzer. Each measurement was repeated thrice.

3. Results and discussion

3.1. Effectiveness of carbon source deposition

The effectiveness of incorporation of the carbon precursor into the silica pore system was determined by means of thermogravimetric measurements under an air atmosphere. The real contents of the precipitated poly(furfuryl alcohol) are shown in Fig. 1.

The efficiency of PFA deposition follows the amount of monomer available in the reaction slurry, thus the real PFA/SiO$_2$ mass ratio for the M48-based composite attains 1.93, while in the case of S1, it equals 1.06. These values correspond to the effectiveness of deposition of around 50 % for both materials and are close to those found for silicas with broader pores, which were investigated in our previous paper [54]. Such an efficiency stems from the loss of part of the toluene-soluble oligo/polymeric forms of PFA during the separation of the composite from the reaction mixture [15,32–34]. It should be noted that despite slightly broader pores in M48 (see Table 2, Fig. 2), this matrix requires a much larger PFA loading to obtain a faithful replica than S1. This is likely due to the complex tortuosity of the gyroid-like channel system of M48, and the consequently hindered diffusion of the monomer molecules throughout its porous structure [10,33]. The relatively large excess of monomer used allowed compensation for this effect, but, *ipso facto*, the loading of the M48 with polymer exceeds the total pore volume of the
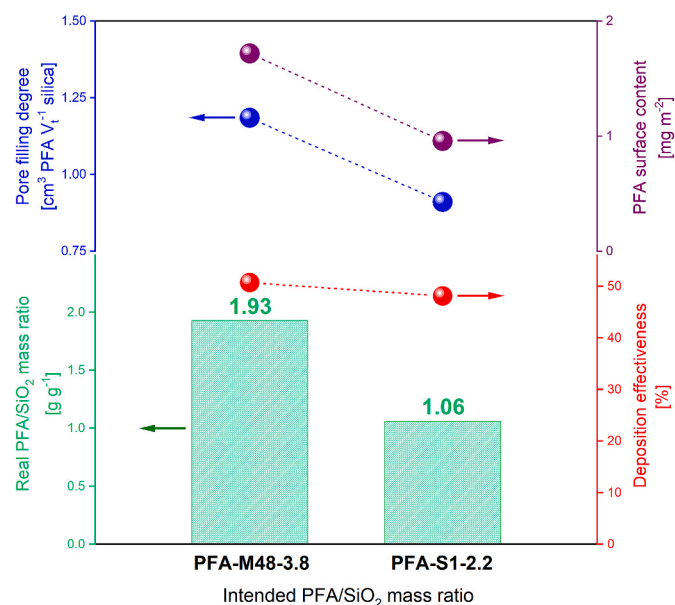

Fig. 1. Effectiveness of the carbon precursor deposition in the silica matrice's pore systems.

matrix (118 %). Contrarily, the incomplete filling of the S1 silica pores (91 %) is also sufficient to provide obtaining a regular structure of the final replica, which may seem somewhat counterintuitive. Yet, this becomes understandable given the thermal shrinkage of silica through carbonization [54]. The surface coverage with 1.72 and 0.96 mg m^{-2} for M48 and S1, respectively, corresponds to the even PFA layer of a nanometer-scale thickness. These remarks are in line with the physisorption measurements. Namely, the nitrogen uptake close to nil for both PFA/SiO$_2$ composites before carbonization clearly corroborates the complete filling of the pore systems thereof (see Fig. 2, Table 2). Meanwhile, the lack of formation of observable polymer cover around the silica particles is evidenced by SEM (Fig. 4). Given the mass loss of PFA itself during carbonization of approximately 54 wt% [34], and the efficiency of polymer deposition in M48 and S1, one can calculate that, starting with 1.00 g of silica, yields of 0.89 g of CMK-1 and 0.49 g of CMK-2 replica can be obtained. This corresponds to 23 % of the mass of the carbon source (with regard to the monomer) in both cases.

3.2. Textural and structural characteristics

3.2.1. Silica templates

The textural and structural features of the materials were investigated at every stage of the nanoreplication route. The low-temperature nitrogen adsorption-desorption isotherms and corresponding pore size distributions (PSDs) for pristine silicas, PFA/SiO$_2$ composites before carbonization, C–Y–x carbonizates, and ultimate replicas are shown in Fig. 2 (for carbons, additionally the isotherms of CO$_2$ adsorption at 0 °C were acquired), while the associated low-angle XRD patterns are displayed in Fig. 3. The calculated textural and structural parameters are compiled in Table 2.

Both isotherms collected for pristine silica matrices show essentially similar shapes of the adsorption branches with steep capillary condensation steps, characteristic of type IV(b), typical of mesoporous materials with small mesochannels [66] (Fig. 2A and B). However, the isotherm for S1 is actually fully reversible (excluding the minute loop at the highest relative pressure), while M48 features the H4 hysteresis loop, revealing the presence of certain inhomogeneities in its structure. The latter presents a narrow distribution of pore size centered at 3.2 nm, though. The S1 material also shows uniformity in pore size distribution at 2.8 nm, however, its PSD is visibly broader than for M48, which arises from the complex geometry of its channel system (cf. Scheme 1).

The micropore volume calculations (Table 2) have shown that both parent silicas are exclusively mesoporous materials with BET apparent surface area exceeding 1100 m^2 g^{-1}, and the total pore volumes of 1.05 and 0.75 cm^3 g^{-1} for M48 and S1, respectively. These values are comparable to those published elsewhere for such structures [10,14,23,33,61,62,67,69–71,73,75–77].

It is pertinent to mention that M48 and S1 silicas, due to their relatively thin walls (cf. Table 2), are easily prone to pronounced high-temperature shrinkage. This is seen in the nitrogen isotherms and PSDs for M48@850 and S1@850 (Fig. 2). Both of them show the shape of type I(b), characteristic of solids having wider micropores and/or narrow mesopores [66]. This is in line with the relevant PSDs featuring a shift towards lower pore sizes on the boundary between the micro- and mesopore ranges. Simultaneously, notable thickening of pore walls is observed (Table 2). Interestingly, the impact of the skeletal contraction on the total pore volume and BET specific surface area is herein roughly 1.7–2.8, and 1.3–2.3 times higher, respectively, with regards to the materials characterized by broader pores and thicker walls like SBA-15, SBA-16, and KIT-6, as we recently reported [54].

The low-angle XRD patterns (see Fig. 3) acquired for parent silica templates confirm the successful synthesis of both desired structures.

The profile for M48 shows two distinct Bragg's reflections at the angular positions of 2.71° and 3.13°, indexed as (1 1 0) and (2 1 1), respectively, characteristic of the bicontinuous interwoven gyroid array (sometimes referred to as a *saddle surface* [75,77], cf. Scheme 1),

Table 2
Textural and structural parameters of the materials calculated from N_2/CO_2 physisorption and X-ray diffraction.

Sample	S_{BET} $S_{2D-NLDFT}$ [a] (S_{ex}, α_s) [m² g⁻¹]	S_μ, t-plot [m² g⁻¹]	V_t, s-p [cm³ g⁻¹]	V_μ, α_s (V_μ, t-plot) $V_{\mu,2D-NLDFT}$ [b] / $V_{\mu,CO2}$ [c] [cm³ g⁻¹]	V_{me}, α_s [cm³ g⁻¹]	D_p [nm]	D_w [nm]	a_0 [nm]	RFI [d] [−]
M48	1122 (97)	0	1.05	0.00 (0.00)	0.92	3.2[e]	0.9[i]	8.0[l]	–
S1	1104 (68)	0	0.75	0.00 (0.00)	0.66	2.8[e]; (4.3)[f]	0.4[j]	8.5[m]	–
M48@850	609 (35)	0	0.30	0.00 (0.00)	0.25	1.8[e]	1.4[i]	6.5[l]	–
S1@850	410 (42)	0	0.21	0.00 (0.00)	0.15	2.1[e]; (2.8)[f]	1.2[j]	7.2[m]	–
PFA–M48–3.8	<10	0	0.01	<0.01 (0.00)	–	–	–	–	–
PFA–S1–2.2	<10	0	<0.01	<0.01 (0.00)	–	–	–	–	–
C–M48–3.8	78 (<10)	48	0.05	0.02 (0.02)	0.01	0.6[g]	–	7.2[l]	–
C–S1–2.2	36 (<10)	20	0.02	0.01 (0.01)	0.00	0.5[g]	–	7.4[m]	–
CMK-1	1607 *1219* (47)	0	0.94	0.08 (0.00) *0.49* 0.13	0.78	0.5; 1.9[h]	2.5[k]	7.2[n]	1.5
CMK-2	1493 *1291* (71)	25	0.86	0.13 (0.04) *0.51* 0.18	0.60	0.5; 1.2[h]	2.2[k]	–[o]	2.4

[a] Specific surface area calculated from N_2 adsorption isotherm using the 2D-NLDFT model (see *Supplementary Information*).

[b] Micropore volume calculated from N_2 isotherm using the 2D-NLDFT model (see *Supplementary Information*).

[c] Micropore volume calculated following the Dubinin-Radushkevich equation (CO_2, adsorption branch) (Fig. S2).

[d] Dimensionless Replication Fidelity Index; details described elsewhere [15,34,54].

[e] Zeolite (H-form)-N2-77, cylindrical model, adsorption branch (SAIEUS ver. 2.02, Micromeritics).

[f] Cage diameter in the S1 structure; $D_{cage} = a_0\left(\frac{3}{4}\frac{\varepsilon_{me}}{\pi}\right)^{1/3}$; ε_{me} – volume fraction of cavities per unit cell; $\varepsilon_{me} = \frac{V_{me}\cdot\rho_s}{1 + V_t\cdot\rho_s}$; ρ_s – amorphous silica density; $\rho_s = 2.2$ g cm⁻³ [67–70].

[g] 2D-NLDFT model for carbons with heterogeneous surfaces (N_2, adsorption branch) [54,55].

[h] Dual gas 2D-NLDFT model for carbons with heterogeneous surfaces (simultaneous fit to the adsorption branches of N_2 and CO_2 isotherms) [58,59].

[i] Average thickness of the M48 wall; $D_w = \frac{a_0}{3.0919}\left(1 - \frac{V_{me}\cdot\rho_s}{1 + V_{me}\cdot\rho_s}\right)$ [14].

[j] Minimal thickness of the S1 wall; $D_{w,min} = a_0\frac{5^{1/2}}{4} - D_{cage}$ [68].

[k] Average thickness of the carbon rods in the replicas calculated based on the linearity of the D_p vs. a_0 relationship for the mesoporous silicas calcined at different temperatures and relevant carbonizates (see Fig. S5; the calculation approach explained in the discussion) [78].

[l] The ($Ia\overline{3}d$) lattice parameter; $a_0 = 6^{1/2}\cdot d_{2\,1\,1}$ [14,61].

[m] The ($Pm\overline{3}n$) lattice parameter; $a_0 = 5^{1/2}\cdot d_{2\,1\,0}$ [67,69,70].

[n] The ($I4_1 32$) lattice parameter; $a_0 = 2^{1/2}\cdot d_{1\,1\,0}$ [14].

[o] Featureless XRD pattern (cf. Fig. 3B).

classified as the cubic $Ia\overline{3}d$ space group [10,14,61,75–77]. Noteworthy, the presence of higher order signals (at $2\theta > 4°$) reveals an excellent long-range ordering of this material, which is consistent with the TEM imaging (cf. Fig. 5). The XRD pattern of S1 shows three partly overlapping reflections at 2θ of 2.11°, 2.33°, and 2.53° described with the Miller indices of (2 0 0), (2 1 0), and (2 1 1), respectively, which confirm the $Pm\overline{3}n$ symmetry of this silica [23,62,67,69–74].

The XRD analysis disclosed that both materials are resistant to high-temperature annealing. Namely, although the contraction is manifested by shifting patterns towards higher 2θ positions, they basically retain the original arrays thereof (viz. Fig. 3). The drop in the lattice parameter of M48@850 is approximately twice as bigger than for SBA-15, SBA-16, and KIT-6 [54], while for S1@850 it is one and a half times higher. The parameters of the high-temperature annealed silicas were used to estimate the thickness of the carbon walls in the ultimate replicas, which will be discussed further.

3.2.2. PFA–Y–x composites and C–Y–x carbonizates

Considering the character of the isotherms measured for the non-carbonized materials, one can see at a glance that loading the silicas' pore system with carbon source brought substantial changes in their porosity. The specific surface areas <10 m² g⁻¹ accompanied by the total pore volumes as low as up to 0.01 cm³ g⁻¹ clearly show that both composites are entirely nonporous (see Fig. 2A and B, Table 2). Referring to the total pore volumes of bare silicas, the level of pore filling with PFA was 98 % and 99 % for M48 and S1, respectively. This suggests the successful incorporation of PFA into the pores of both silica templates. Furthermore, N_2 isotherms and XRD patterns for the carbonizates (viz. Figs. 2 and 3) reveal that carbonization brought further alteration in textural and structural parameters. The isotherms of I(b) type [66] featuring the adsorbate uptake vastly lower compared with respective bare silicas reveal still almost complete extinction of the mesopores (up to 93–97 %). Moreover, the template shrinking down around the organic material coinciding with the carbonization process causes the voids inside the C–S1–2.2 composite to disappear (cf. Fig. 1 – pore filling degree vs. Fig. 2A – isotherms with the N_2 uptake close to nil). The residual porosity in carbonizates is commonly ascribed to the slit micropores which appear at the carbon-silica interface due to their detachment caused by a divergence in the scale of their thermal shrinkage (Table 2, Fig. 2A', B'; note that both bare silicas are purely mesoporous) [15,32, 54,55].

3.2.3. Carbon replicas

The nitrogen adsorption isotherms and respective PSDs for the ultimate carbon replicas are presented in Fig. 2, while the corresponding XRD patterns are shown in Fig. 3. It is observed that the removal of the silica matrices from the carbonizates leads to opening up the porosity of the materials. Basically, one can infer that in the case of the CMK-1 replica, the type of isotherm corresponds to that of the bare matrix, i. e. it is of type IV(b) with a vastly tight H4 hysteresis loop (narrower than for silica; see Fig. 2A) [66]. This points to the excellent uniformity of the pore shape and size of this replica. The abrupt nitrogen uptake at the
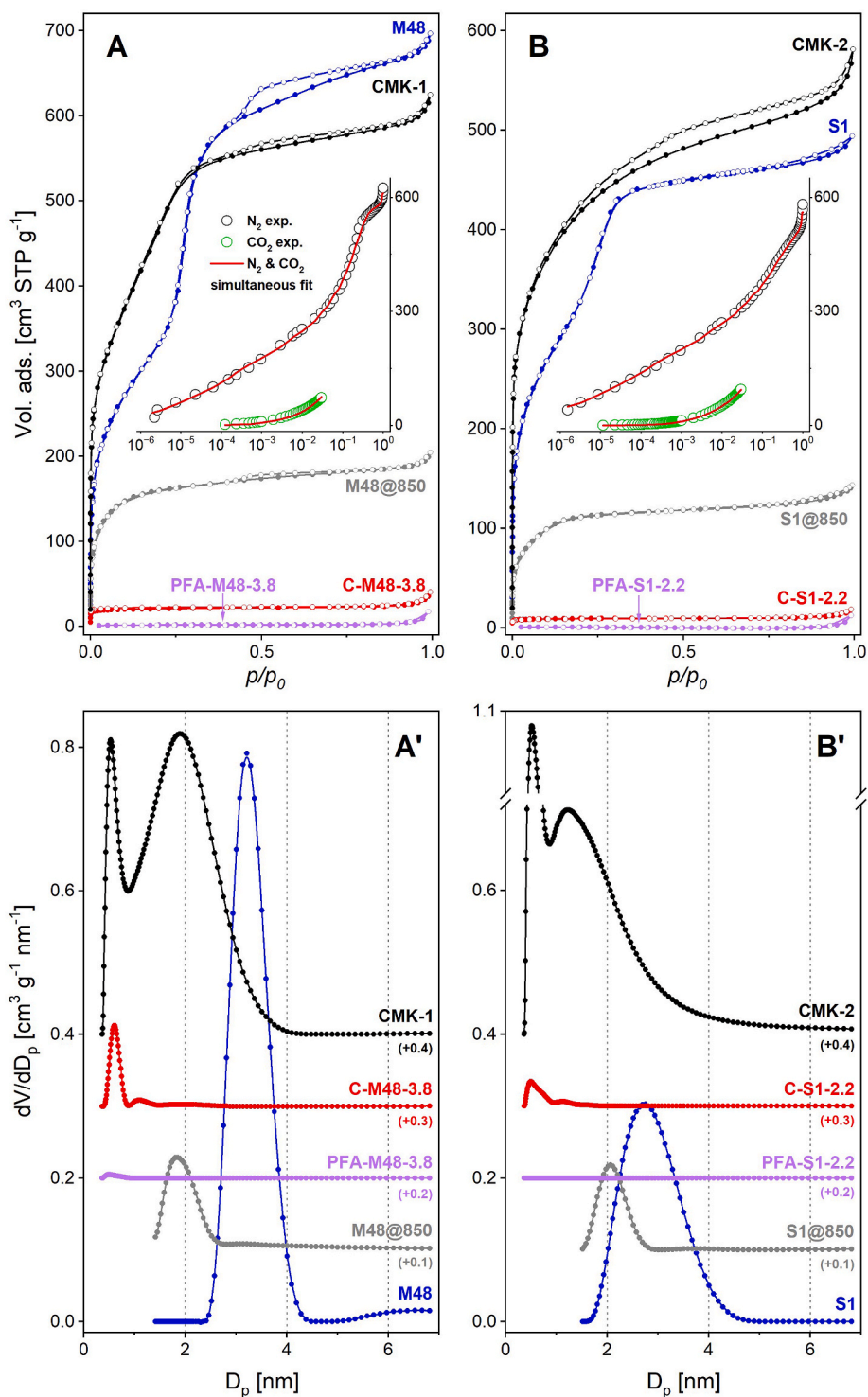
Fig. 2. N_2 adsorption-desorption isotherms (closed and open symbols, respectively) for the parent silicas and their counterparts annealed at 850 °C (blue and grey lines and symbols, respectively), PFA/SiO$_2$ composites before carbonization (violet), carbonizates (red), and corresponding carbon replicas (black) for the M48-and S1-based series (A and B, respectively). Insets: experimental adsorption isotherms of N_2 and CO_2 for carbon replicas and simultaneous fit of the NLDFT models. The corresponding PSDs are depicted in panels A' and B' (the respective colours maintained; the vertical shifts in parentheses). For the PSDs calculation details refer to *Supplementary Information*.

lowest relative pressure (up to 10^{-2}) suggests that the total pore volume is contributed by a certain portion of micropores. Noteworthy, the low-pressure region of the isotherm discloses the amorphous character of the carbonaceous material itself (otherwise, the semi-logarithmic-scale plotted isotherms should feature a characteristic S-shaped fragment at the $p/p_0 = 10^{-5}$–10^{-3}, pointing to the

layer-by-layer N_2 adsorption on a graphitized material [54,57,79]; cf. Fig. 2A, B, and Fig. S3). This is understandable given the relatively mild conditions of carbonization. The further steep segment of the adsorption branch with a sharp *knee* at $p/p_0 = 0.3$ corresponds to the capillary condensation of the adsorbate in narrow and size-wise uniform mesopores. The slight slope of the isotherm at $p/p_0 > 0.3$ suggests the
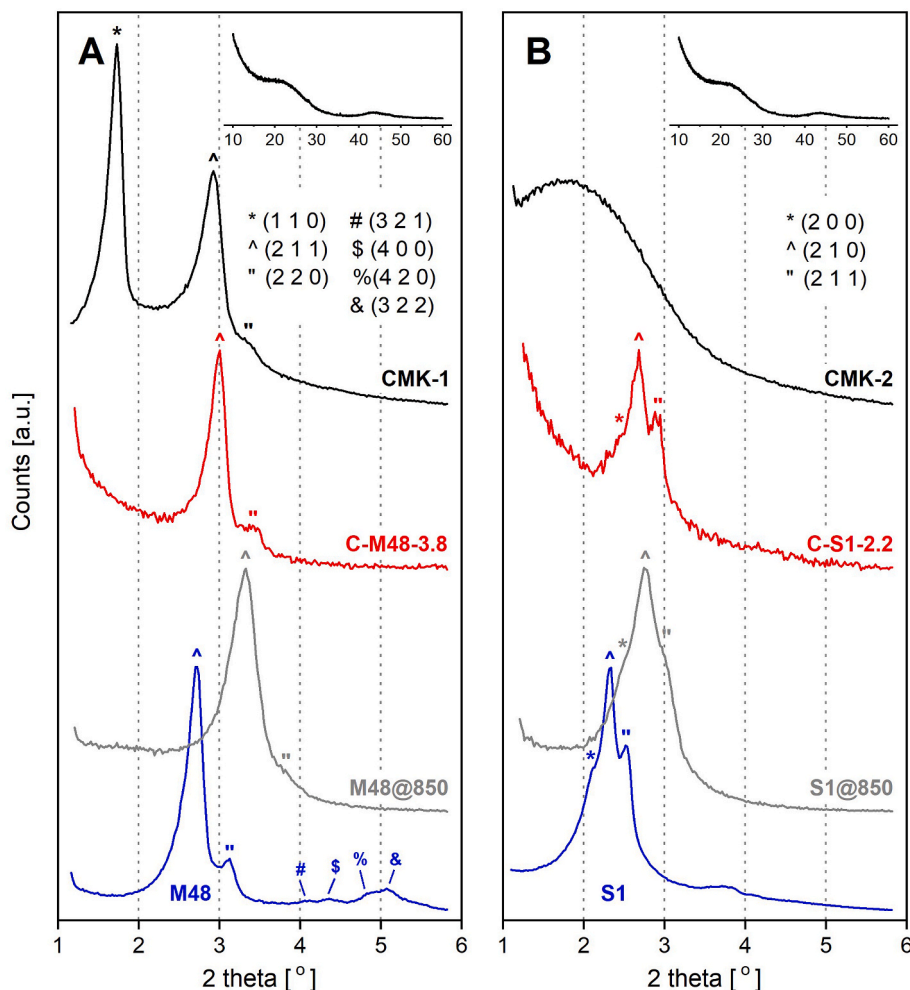
Fig. 3. Low-angle X-ray diffraction patterns for silicas (blue and grey lines), carbonizates (red), and corresponding carbon replicas (black) recorded for M48-and S1-based series (A and B, respectively). Insets: patterns recorded at 10.00–60.00° 2θ for the replicas. Intensity normalization: $1 \propto I_{(2\,1\,1)}$ (A), $1 \propto I_{(2\,1\,0)}$ (B).

relatively small external surface area of this material that is of the same order of magnitude as M48@850 (cf. Table 2). This in turn is a certain premise supporting the retention of the particle morphology through all stages of the nanoreplication procedure.

This is not the case with the replication of the S1 material. Namely, the behavior of the isotherm alternates from reversible IV(b) shape for the parent silica towards the I(b) type with a relatively broad H4 hysteresis for CMK-2, which is typical for the materials having channels on the boundary between micro- and mesopores [66] (Fig. 2B). The presence of the hysteresis loop is due to the geometry of the CMK-2 pores, which is more complex than for CMK-1 (see Scheme 1). Nonetheless, similarly to CMK-1, the CMK-2 replica also shows appreciable adsorption at the lowest relative pressures (again, there is a lack of graphitization), and the external surface comparable to the mother silica. The basic textural parameters for both synthesized replicas stand within typical values reported elsewhere (for CMK-1 S_{BET} = 1200–1800 m² g⁻¹, V_t = 0.9–1.2 cm³ g⁻¹ [12]; for CMK-2 S_{BET} = 1447–1934 m² g⁻¹, V_t = 0.8–1.17 cm³ g⁻¹ [18,23]). The specific surface areas calculated from the 2D-NLDFT model fitted to nitrogen isotherm are noticeably lower than S_{BET} (Table 2), but they appear to be more accurate given the limitations of the BET model [2]. Contrarily, the corresponding micropore volumes seem to be definitely overestimated in view of the CO_2 adsorption-based values (the latter are considered sounder according to IUPAC [66]).

It should be underscored that it is necessary to be cautious when analyzing the pore size distribution for materials that feature pores of

size around the micro- and mesopore threshold. This stems from two factors, i.e. (i) underequilibration of the nitrogen isotherms in the micropore region caused by its slow diffusion at cryogenic temperatures [58,59], and (ii) limited applicability of the available PSD calculation models (be it the formerly used BJH and the more recent DFT approaches) due to the slit-cylinder shape boundary arbitrarily set at 2 nm [59]. The former circumstance entails the underestimation of micropore volume, while the latter additionally results in certain inherent artifacts on the PSDs [58,59]. Additionally, in view of the aforementioned, also, the micropore volumes computed on the nitrogen isotherm are merely indicative; in fact, regardless of the calculation model used they are underestimated (though, this is particularly evident when using the *t*-plot model [58,59,80], cf. Fig. S1, Table 2). For this reason, we measured the isotherms of carbon dioxide adsorption at 0 °C, which, contrarily to N_2, are truly equilibrated due to the fast diffusion of the adsorptive. Based on the Dubinin-Radushkevich equation, we calculated the reliable micropore volumes ($V_{\mu,CO2}$; Table 2 and Fig. S2) [54]. As anticipated, both replicas feature a mixed micro-mesoporous character with abundant micropore shares (14 and 21 % for CMK-1 and CMK-2, respectively). Such a nature was previously found for all the *rod-type* mesostructures (i.e. those derived from composites fully filled with a carbon precursor) [54].

Furthermore, we applied the simultaneous fitting of the NLDFT models to the CO_2 and N_2 adsorption data for the calculation of the PSDs following the dual gas approach proposed recently [58,59]. The experimental adsorption data together with the simultaneous fits of the
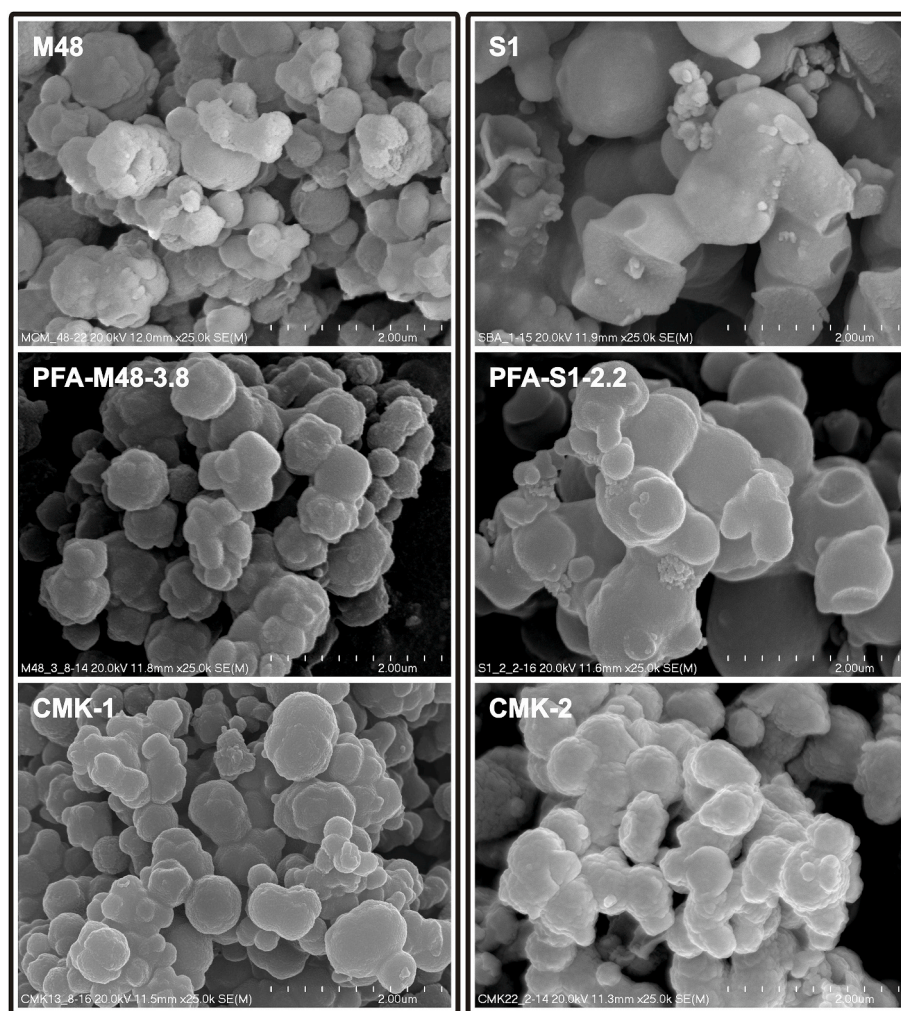
Fig. 4. SEM images of the silica templates (top), non-carbonized PFA/SiO$_2$ composites (middle), and corresponding carbon replicas (bottom).

relevant 2D-NLDFT models are shown as the insets in Fig. 2A and B. The robust fitting of these models led to achieving reliable PSDs curves (displayed in Fig. 2A', B'). As seen, both replicas reveal bimodal PSDs with the micropore size centered at 0.5 nm (this is the indigenous ultramicroporosity of the carbonized polymer itself), and broader pores at 1.9 and 1.2 nm for CMK-1 and CMK-2, respectively, formed in the place of the leached silica. It should be noted that these sizes are lower than those reported previously (3.0 and 1.8–3.0 nm for CMK-1 and CMK-2, respectively [12,18,23]), which can be explained by the discrepancies in the calculation models used. The PSD tailing towards bigger sizes observed for the CMK-2 material is due to the more complex shape of its pores than CMK-1.

In order to illustrate the importance of the careful analysis of the discussed PSDs region, we intentionally calculated them based exclusively on the single adsorbate isotherm (nitrogen) and plotted them comparatively against the dual gas-calculated ones (see Fig. S3). Although both models feature an excellent and seemingly identical fitting to the isotherms, the differences in the PSDs shapes are unambiguous (noteworthy, the superb fit within the entire relative pressures seen in the N$_2$ adsorption isotherms proves the suitability of the use of the dual gas tool). Namely, both single gas-based PSDs show an evidently artificial peak centered at around 1 nm. Meanwhile, a simple geometrical deliberation clearly indicates that the bimodality of CMK-1 and CMK-2 replicas should definitely be ruled out despite the tortuosity of pore systems thereof (viz. Scheme 1). This justifies the necessity to measure the adsorption isotherms of both CO$_2$ and N$_2$ and depicts the

usefulness of the dual gas approach for such materials [58,59].

Interesting insights are provided by comparing the mean pore sizes of replicas with the wall thicknesses of the corresponding silicas calcined at 850 °C (Table 2). For the CMK-2 material, they correlate excellent (both wall thickness of S1@850 and the pore size of CMK-2 equal 1.2 nm), which is understandable given the integrity of its carbon skeleton. In contrast, for the CMK-1 replica, the discrepancy is more pronounced (for M48@850 D$_w$= 1.4 nm; for CMK-1 D$_p$=1.9 nm). This, however, should not be surprising when considering the rearrangement of the carbon symmetry upon silica removal, as proven by the XRD pattern (Fig. 3, Scheme 1).

The low-angle XRD pattern for the CMK-1 mesostructure (Fig. 3A) shows three well-distinguished signals, two of which are inherited from the carbonizate and keep their angular positions (i.e. (2 1 1) and (2 2 0)). The third, newly appearing sharp reflection of a dominant intensity observed at 1.72° and indexed as (1 0 0) is symmetrically forbidden for the $Ia\bar{3}d$ space group [10,49]. Thus, its emergence proves the lowering of the symmetry of the material to $I4_132$ upon removal of silica, which arises from the displacement of the two interwoven (but not merged to each other) carbon sub-frameworks of the CMK-1 replica. It was supposed elsewhere that this displacement occurs most likely along the [1 1 0] direction (without distortion and rotation), thus providing the structure with the least degree of freedom (Scheme 1) [22,56]. Nevertheless, the intensity of all the signals discloses the excellent ordering of the material and its structural homogeneity.

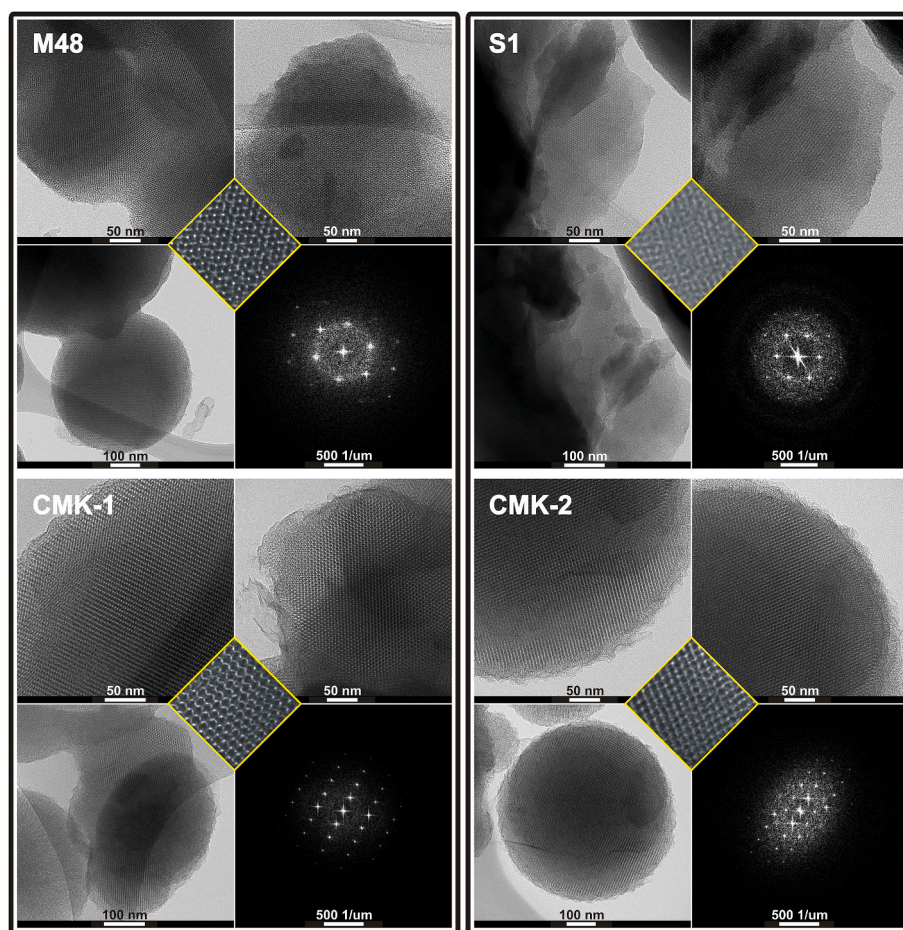Surprisingly, counter to Babinet's principle, the CMK-2 structure

Fig. 5. TEM images and Fourier diffractograms of the silica templates (top), and their respective carbon analogues (bottom).

exhibits a single, broad XRD peak centered at 1.8° 2θ (Fig. 3B). At first glance, this could suggest a fiasco of the synthesis of the regular CMK-2 structure, but this, in turn, contradicts the results of physisorption and SEM and TEM imaging (as discussed further). Yet, a similar effect has already been reported (but not unraveled) by others [10]. A plausible explanation may be the formation of an amorphous carbon cover enveloping the material's particles around. Indeed, by analyzing a series of TEM images of this replica, we found a recurring motif of such a cladding (viz. Fig. S4). This 'shell' may shield the ordered 'core' of the grain against the X-rays and distort the pattern, as was discussed elsewhere [54]. The presence of the shell is also reflected in the high value of the Replication Fidelity Index (RFI = 2.4; cf. Table 2). In our former paper, we report that RFI >1 is typical of materials in which the outer particle's surface is clad with a disordered carbon cover [15]. Perhaps, the tendency to form such cladding is related to the concentration of free superficial silanols on the silica grains, which are capable of covalently binding the carbon precursor [54,55]. Furthermore, the formation of a separate fraction of the amorphous carbon phase aside from the silica particles cannot also be ruled out. In order to fully address this investigation-worthy issue, additional analyses are needed though. The wide-angle XRD patterns collected for both studied carbon replicas (Fig. 3, insets) show the amorphous nature of the carbonaceous material itself, notwithstanding the silica matrix used. The lack of characteristic signals at 26°, 43°, and 54° 2θ clearly points to the absence of graphitic species [79].

The approximate mean wall thickness of the carbon replicas was assessed by combining the textural and structural data for the mother silicas, their high-temperature annealed counterparts, and carbonizates. These estimates are based on the assumption of the linearity of the pore

size vs. lattice parameter relationship for silica mesostructures calcined at different temperatures, which was reported by others [78]. As stated above, both carbonizates keep the symmetry of the pristine silicas, but their thermal shrinkage is evident (Fig. 3). In both cases, the lattice parameter falls within the a_0 values for pristine and high-temperature treated silicas (cf. Table 2, Fig. 3). This means that the carbon precursor deposit inside pores plays the role of a filler acting against the deeper contraction of the silica array and additionally confirms the successful incorporation of PFA. Therefore, by plotting the linear relationship $D_p = f(a_0)$ for silicas and carbonizates, one can easily extract the average wall thickness of the replicas (see Fig. S5). As shown in Table 2, the walls of both materials are thick enough to provide them with sufficient rigidity (2.5 and 2.2 nm for CMK-1 and CMK-2, respectively).

3.3. Morphology and phase purity

The morphology and structural arrangement of the final carbon replicas against the bare silica matrices and non-carbonized polymer/ SiO_2 composites were investigated by scanning and transmission microscopy. The examples of SEM and TEM micrographs are presented in Figs. 4 and 5, respectively.

As seen in Fig. 4, both silicas reveal a roughly spherical grain morphology with largely coalesced particles, which is in line with the previous reports [56,67,70–76]. Noteworthy, the M48 matrix exhibits a visibly smaller particle diameter than S1 (approx. 0.5–1.0 μm vs. 1.0–2.0 μm, respectively). The images for non-carbonized composites disclose a lack of formation observable superficial or separate self-aggregated polymer species. Finally, when analyzing the images taken for the carbons, one can see that the primary morphology was

perfectly preserved.

The TEM micrographs and Fourier diffractograms for the pristine silicas (Fig. 5) clearly confirm their cubic arrays and excellent regularity (homogeneity) over their whole grains. It should be noted that the careful analysis of dozens of other images (not shown here) revealed a lack of any disordered impurities in both materials, which is in line with the excellent textural and structural parameters discussed above.

The daughter carbon mesostructures also reveal the long-range ordering (Fig. 5). Due to the integrity of its carbon framework, the CMK-2 material is an exact negative structure of the S1 matrix [23]. Similarly, the CMK-1 is a faithful analogue of the M48 silica, but the displacement of its carbon sub-frameworks can be explicitly seen in the inset presented in Fig. 5 (see the regular pattern for M48 vs. the image with brighter and darker parallel *zigzags* for CMK-1; this was thoroughly discussed elsewhere [22]).

The phase purity of the studied replicas was investigated non-directly following the approach based on the measurements of thermal stability [54,55,57,79]. For this purpose, we performed high-resolution thermogravimetric analyses under an air atmosphere (the steeper the TG curve and narrower DTG, the higher the homogeneity of the oxidized material itself). The acquired results are shown in Fig. S6. Both materials show vastly narrow DTG curves, which evidence the high homogeneity of their structures. The maximum oxidation rate, corresponding to the combustion of amorphous carbonaceous material with a lack of measurable degree of graphitization, was observed at 555 °C [54,55,57, 79]. Overall, the similarity in the thermal stability of CMK-1 and CMK-2 is not surprising considering the same starting carbon precursor, synthesis pathway used, and their comparable wall thicknesses and pore sizes. The TG measurements also reveal the vestigial content of the residual silica in the ultimate materials. The elemental analysis allowed us to calculate the average empirical formulas of $C_{10.0}H_{1.4}O_{0.5}$ and $C_{10.0}H_{1.5}O_{0.8}$ for CMK-1 and CMK-2, respectively (Table S2). This remains consent with the mean composition of similar *rod-type* carbon replicas such as CMK-3, 6, and 8, as we have reported recently [54].

4. Conclusion

A facile procedure for carbon nanoreplication of silica matrices with narrow mesopores has been developed. This method is reproducible and operates under mild conditions using basic laboratory equipment and renewable carbon precursor (FA is produced from hydrolyzed biomass waste). The principle of the synthesis is the solvent-polarity-controlled deposition of poly(furfuryl alcohol) as a carbon source on the unmodified silica in a non-polar medium. The polymer insertion is a self-regulating process governed by the favored anchoring of monomer molecules on the free silanols. This way, even coverage of the matrix surface with polymer is provided, leading to the formation of faithful negative carbon mesostructures of outstanding structural homogeneity and long-range ordering while retaining the primary grain morphology.

Following this procedure, we synthesized the CMK-1 and CMK-2 materials cast from MCM-48 and SBA-1 silicas, respectively. Both carbons reveal excellent textural and structural parameters surpassing quality-wise the majority of suchlike materials that have been reported thus far. Furthermore, the in-depth textural characterization disclosed that they feature a mixed micro-mesoporous character of the carbonaceous matter itself (to the best of our knowledge, herein we provided the exhaustive textural characterization of the CMK-2 structure for the first time). We believe this research paves the way for the manufacturing and application of CMK-1 and CMK-2 carbon replicas on a larger scale.

Besides, it was found that the analysis of physisorption data using the dual gas approach (simultaneous N_2 and CO_2 2D-NLDFT models fitting) offers a comprehensive textural characterization of the carbon mesostructures under study. It is useful for the calculation of reliable pore size distributions, particularly for the solids with pore sizes on the boundary between micro- and mesopores, as it allows for the extraction of PSDs rectified from the inherent artifacts appearing in this region. This is of great importance for the thorough characterization of similar materials. Therefore, recording both N_2 and CO_2 isotherms combined with using a dual gas calculation tool is strongly recommended.

The present research gives rise to anticipate that the developed concept could also be feasible in the synthesis of other negative carbon mesostructures (e.g. CMK-4) and, perhaps, even microporous solids (e.g. large-pore zeolites). This will be the concern of the forthcoming research.

CRediT authorship contribution statement

R.J.: Conceptualization, Synthesis, Characterization, Writing – original manuscript, review & editing, Visualization, Formal analysis, Funding acquisition, Project administration. **S.J.:** Characterization, Writing – original manuscript, review & editing. **J.J.:** Calculation and interpretation of textural parameters, Writing – original manuscript, review & editing. **P.N.:** Characterization, Writing – original manuscript, review & editing. **M.W.:** Writing – original manuscript, review & editing. **M.L.:** Writing – original manuscript, review & editing. **M.M.:** Characterization, Writing – original manuscript, review & editing. **P.K.:** Writing – original manuscript, review & editing.

Declaration of competing interest

The authors declare that they have no known competing financial interests or personal relationships that could have appeared to influence the work reported in this paper.

Acknowledgments

Appendix A. Supplementary data

Supplementary data to this article can be found online at https://doi.org/10.1016/j.carbon.2023.118575.

References

[1] G.S. Day, H.F. Drake, H.C. Zhou, M.R. Ryder, Evolution of porous materials from ancient remedies to modern frameworks, Commun. Chem. 4 (2021) 2–5, https://doi.org/10.1038/s42004-021-00549-4.

[2] H. Marsh, et al., Characterization of porosity: immersion calorimetry, in: H. Marsh, F. Rodríguez-Reinoso (Eds.), Activated Carbon, first ed., Elsevier, 2006, p. 209, https://doi.org/10.1016/b978-008004463-5/50018-2.

[3] H. Ghaedi, M. Zhao, Review on template removal techniques for synthesis of mesoporous silica materials, Energy Fuel. 36 (2022) 2424–2446, https://doi.org/10.1021/acs.energyfuels.1c04435.

[4] M.R. Benzigar, S.N. Talapaneni, S. Joseph, K. Ramadass, G. Singh, J. Scaranto, U. Ravon, K. Al-Bahily, A. Vinu, Recent advances in functionalized micro and mesoporous carbon materials: synthesis and applications, Chem. Soc. Rev. 47 (2018) 2680–2721, https://doi.org/10.1039/c7cs00787f.

[5] Q. Wang, D. Astruc, State of the art and prospects in metal-organic framework (MOF)-based and MOF-derived nanocatalysis, Chem. Rev. 120 (2020) 1438–1511, https://doi.org/10.1021/acs.chemrev.9b00223.

[6] A.E. Baumann, D.A. Burns, B. Liu, V.S. Thoi, Metal-organic framework functionalization and design strategies for advanced electrochemical energy storage devices, Commun. Chem. 2 (2019) 1–14, https://doi.org/10.1038/s42004-019-0184-6.

[7] A. Thomas, Much ado about nothing – a decade of porous materials research, Nat. Commun. 11 (2020) 11–13, https://doi.org/10.1038/s41467-020-18746-5.

[8] H. Sun, Z. Xu, C. Gao, Multifunctional, ultra-flyweight, synergistically assembled carbon aerogels, Adv. Mater. 25 (2013) 2554–2560, https://doi.org/10.1002/adma.201204576.

[9] I.M. Hönicke, I. Senkovska, V. Bon, I.A. Baburin, S. Bönisch, S. Raschke, J. D. Evans, S. Kaskel, Balancing mechanical stability and ultrahigh porosity in crystalline framework materials, Angew. Chem. Int. Ed. 57 (2018) 13780–13783, https://doi.org/10.1002/anie.201808240.

[10] R. Ryoo, S.H. Joo, S. Jun, Synthesis of highly ordered carbon molecular sieves via template-mediated structural transformation, J. Phys. Chem. B 103 (1999) 7743–7746, https://doi.org/10.1021/jp991673a.

[11] B. Szczęśniak, J. Choma, M. Jaroniec, Major advances in the development of ordered mesoporous materials, Chem. Commun. 56 (2020) 7836–7848, https://doi.org/10.1039/d0cc02840a.

[12] R. Ryoo, S.H. Joo, Nanostructured carbon materials synthesized from mesoporous silica crystals by replication, in: Stud. Surf. Sci. Catal., Elsevier Inc., 2004, pp. 241–260, https://doi.org/10.1016/s0167-2991(04)80200-3.

[13] C. Vix-Guterl, S. Boulard, J. Parmentier, J. Werckmann, J. Patarin, Formation of ordered mesoporous carbon material from a silica template by a one-step chemical vapour infiltration process, Chem. Lett. (2002) 1062–1063, https://doi.org/10.1246/cl.2002.1062.

[14] M. Kruk, M. Jaroniec, R. Ryoo, S.H. Joo, Characterization of ordered mesoporous carbons synthesized using MCM-48 silicas as templates, J. Phys. Chem. B 104 (2000) 7960–7968, https://doi.org/10.1021/jp000861u.

[15] R. Janus, P. Natkański, M. Wądrzyk, B. Dudek, M. Gajewska, P. Kuśtrowski, Synthesis of *pseudo*-CMK-3 carbon replicas by precipitation polycondensation of furfuryl alcohol in the pore system of SBA-15 detemplated using KMnO₄, Mater. Today Commun. 13 (2017) 6–22, https://doi.org/10.1016/j.mtcomm.2017.07.009.

[16] P. Janus, R. Janus, P. Kuśtrowski, S. Jarczewski, A. Wach, A.M. Silvestre-Albero, F. Rodríguez-Reinoso, Chemically activated poly(furfuryl alcohol)-derived CMK-3 carbon catalysts for the oxidative dehydrogenation of ethylbenzene, Catal. Today 235 (2014) 201–209, https://doi.org/10.1016/j.cattod.2014.03.019.

[17] S.B. Yoon, J.Y. Kim, J.S. Yu, Synthesis of highly ordered nanoporous carbon molecular sieves from silylated MCM-48 using divinylbenzene as precursor, Chem. Commun. (2001) 559–560, https://doi.org/10.1039/b009691l.

[18] A. Vinu, M. Hartmann, Characterization and microporosity analysis of mesoporous carbon molecular sieves by nitrogen and organics adsorption, Catal. Today 102–103 (2005) 189–196, https://doi.org/10.1016/j.cattod.2005.02.028.

[19] J. Yu, W. Du, F. Zhao, B. Zeng, High sensitive simultaneous determination of catechol and hydroquinone at mesoporous carbon CMK-3 electrode in comparison with multi-walled carbon nanotubes and Vulcan XC-72 carbon electrodes, Electrochim. Acta 54 (2009) 984–988, https://doi.org/10.1016/j.electacta.2008.08.029.

[20] H. Huwe, M. Fröba, Synthesis and characterization of transition metal and metal oxide nanoparticles inside mesoporous carbon CMK-3, Carbon 45 (2007) 304–314, https://doi.org/10.1016/j.carbon.2006.09.021.

[21] S.H. Joo, S. Jun, R. Ryoo, Synthesis of ordered mesoporous carbon molecular sieves CMK-1, Microporous Mesoporous Mater. 44 (45) (2001) 153–158, https://doi.org/10.1016/S1387-1811(01)00179-2.

[22] L.A. Solovyov, V.I. Zaikovskii, A.N. Shmakov, O.V. Belousov, R. Ryoo, Framework characterization of mesostructured carbon CMK-1 by X-ray powder diffraction and electron microscopy, J. Phys. Chem. B 106 (2002) 12198–12202, https://doi.org/10.1021/jp0257653.

[23] H. Li, Y. Sakamoto, Y. Li, O. Terasaki, M. Thommes, S. Che, Synthesis of carbon replicas of SBA-1 and SBA-7 mesoporous silicas, Microporous Mesoporous Mater. 95 (2006) 193–199, https://doi.org/10.1016/j.micromeso.2006.05.014.

[24] R. Janus, M. Wądrzyk, P. Natkański, P. Cool, P. Kuśtrowski, Dynamic adsorption-desorption of methyl ethyl ketone on MCM-41 and SBA-15 decorated with thermally activated polymers, J. Ind. Eng. Chem. 71 (2019) 465–480, https://doi.org/10.1016/j.jiec.2018.12.004.

[25] R. Janus, A. Wach, P. Kuśtrowski, B. Dudek, M. Drozdek, A.M. Silvestre-Albero, F. Rodríguez-Reinoso, P. Cool, Investigation on the low-temperature transformations of poly(furfuryl alcohol) deposited on MCM-41, Langmuir 29 (2013) 3045–3053, https://doi.org/10.1021/la3041852.

[26] V.K. Saini, M. Andrade, M.L. Pinto, A.P. Carvalho, J. Pires, How the adsorption properties get changed when going from SBA-15 to its CMK-3 carbon replica, Sep. Purif. Technol. 75 (2010) 366–376, https://doi.org/10.1016/j.seppur.2010.09.006.

[27] J. Goscianska, A. Olejnik, A. Ejsmont, A. Galarda, S. Wuttke, Overcoming the paracetamol dose challenge with wrinkled mesoporous carbon spheres, J. Colloid Interface Sci. 586 (2021) 673–682, https://doi.org/10.1016/j.jcis.2020.10.137.

[28] Z. Ezzeddine, I. Batonneau-Gener, Y. Pouilloux, H. Hamad, Removal of methylene blue by mesoporous CMK-3: kinetics, isotherms and thermodynamics, J. Mol. Liq. 223 (2016) 763–770, https://doi.org/10.1016/j.molliq.2016.09.003.

[29] C.M. Tseng, H.L. Chen, S.N. Lai, M.S. Chen, C.J. Peng, C.J. Li, W.H. Hung, Investigation of free-standing plasmonic mesoporous Ag/CMK-8-Nafion composite membrane for the removal of organic pollutants with 254-nm UV irradiation, Nanoscale Res. Lett. 12 (2017) 362, https://doi.org/10.1186/s11671-017-2124-7.

[30] N. Kiomarsipour, M. Alizadeh, M. Alizadeh, K. Ghani, Synthesis and surface-functionalizing of ordered mesoporous carbon CMK-3 for removal of nitrate from aqueous solution as an effective adsorbent, Diam. Relat. Mater. 116 (2021), 108419, https://doi.org/10.1016/j.diamond.2021.108419.

[31] P. Tan, Y. Jiang, L.B. Sun, X.Q. Liu, K. Albahily, U. Ravon, A. Vinu, Design and fabrication of nanoporous adsorbents for the removal of aromatic sulfur compounds, J. Mater. Chem. A 6 (2018) 23978–24012, https://doi.org/10.1039/c8ta09184f.

[32] P. Niebrzydowska, R. Janus, P. Kuśtrowski, S. Jarczewski, A. Wach, A.M. Silvestre-Albero, F. Rodríguez-Reinoso, A simplified route to the synthesis of CMK-3 replica based on precipitation polycondensation of furfuryl alcohol in SBA-15 pore system, Carbon 64 (2013) 252–261, https://doi.org/10.1016/j.carbon.2013.07.060.

[33] S. Jarczewski, M. Drozdek, A. Wach, B. Dudek, P. Kuśtrowski, M.E. Casco, F. Rodríguez-Reinoso, Oxidative dehydrogenation of ethylbenzene over poly (furfuryl alcohol)-derived CMK-1 carbon replica, Catal. Lett. 146 (2016) 1231–1241, https://doi.org/10.1007/s10562-016-1748-z.

[34] P. Janus, R. Janus, B. Dudek, M. Drozdek, A. Silvestre-Albero, F. Rodríguez-Reinoso, P. Kuśtrowski, On mechanism of formation of SBA-15/furfuryl alcohol-derived mesoporous carbon replicas and its relationship with catalytic activity in oxidative dehydrogenation of ethylbenzene, Microporous Mesoporous Mater. 299 (2020), 110118, https://doi.org/10.1016/j.micromeso.2020.110118.

[35] P. Kuśtrowski, R. Janus, P. Niebrzydowska, Method of synthesis of CMK-3-type carbon replica, U.S. Patent 9,302,252 B2 (April 5, 2016).

[36] X. Niu, X. Wang, K. Guan, Q. Wei, H. Liu, Preparation and electrochemical hydrogen storage application of mesoporous carbon CMK-3 coated Co₂B alloy composite, Chem. Phys. Lett. 778 (2021), 138762, https://doi.org/10.1016/j.cplett.2021.138762.

[37] W. Su, X. Lu, F. Sheng, Y. Sun, C. Liu, G. He, J. Liu, X. Wang, CO₂ sorption properties over ordered mesoporous carbon CMK-3 in the presence of MDEA solution, J. Chem. Eng. Data 63 (2018) 4779–4785, https://doi.org/10.1021/acs.jced.8b00798.

[38] Y. Wang, X. Bai, F. Wang, H. Qin, C. Yin, S. Kang, X. Li, Y. Zuo, L. Cui, Surfactant-assisted nanocasting route for synthesis of highly ordered mesoporous graphitic carbon and its application in CO₂ adsorption, Sci. Rep. 6 (2016), 26673, https://doi.org/10.1038/srep26673.

[39] J. Kochana, K. Wapiennik, P. Knihnicki, A. Pollap, P. Janus, M. Oszajca, P. Kuśtrowski, Mesoporous carbon-containing voltammetric biosensor for determination of tyramine in food products, Anal. Bioanal. Chem. 408 (2016) 5199–5210, https://doi.org/10.1007/s00216-016-9612-y.

[40] C. Weinberger, S. Ren, M. Hartmann, T. Wagner, D. Karaman, J.M. Rosenholm, M. Tiemann, Bimodal mesoporous CMK-5 carbon: selective pore filling with sulfur and SnO₂ for lithium battery electrodes, ACS Appl. Nano Mater. 1 (2018) 455–462, https://doi.org/10.1021/acsanm.7b00307.

[41] K. Yan, X. Sun, S. Ying, W. Cheng, Y. Deng, Z. Ma, Y. Zhao, X. Wang, L. Pan, Y. Shi, Ultrafast microwave synthesis of rambutan-like CMK-3/carbon nanotubes nanocomposites for high-performance supercapacitor electrode materials, Sci. Rep. 10 (2020) 6227, https://doi.org/10.1038/s41598-020-63204-3.

[42] M.V. Kiamahalleh, A. Mellati, S.A. Madani, P. Pendleton, H. Zhang, S.H. Madani, Smart carriers for controlled drug delivery: thermosensitive polymers embedded in ordered mesoporous carbon, J. Pharmaceut. Sci. 106 (2017) 1545–1552, https://doi.org/10.1016/j.xphs.2017.02.010.

[43] Q. Zhao, Y. Lin, N. Han, X. Li, H. Geng, X. Wang, Y. Cui, S. Wang, Mesoporous carbon nanomaterials in drug delivery and biomedical application, Drug Deliv. 24 (2017) 94–107, https://doi.org/10.1080/10717544.2017.1399300.

[44] D. Pavlenko, D. Giasafaki, G. Charalambopoulou, E. Van Geffen, K.G.F. Gerritsen, T. Steriotis, D. Stamatialis, Carbon adsorbents with dual porosity for efficient removal of uremic toxins and cytokines from human plasma, Sci. Rep. 7 (2017) 1–7, https://doi.org/10.1038/s41598-017-15116-y.

[45] X. Peng, S.K. Jain, Understanding the influence of pore heterogeneity on water adsorption in realistic molecular models of activated carbons, J. Phys. Chem. C 122 (2018) 28702–28711, https://doi.org/10.1021/acs.jpcc.8b09143.

[46] X. Peng, J.M. Vicent-Luna, S.K. Jain, Q. Jin, J.K. Singh, Computational study of the effect of functional groups on water adsorption in mesoporous carbons: implications for gas adsorption, ACS Appl. Nano Mater. 2 (2019) 7103–7113, https://doi.org/10.1021/acsanm.9b01633.

[47] W. Schmidt, H. Amenitsch, High dynamics of vapor adsorption in ordered mesoporous carbon CMK-5: a small angle X-ray scattering study, J. Phys. Chem. C 124 (2020) 21418–21425, https://doi.org/10.1021/acs.jpcc.0c05356.

[48] C. Weinberger, M. Hartmann, S. Ren, T. Sandberg, J.H. Smått, M. Tiemann, Selective pore filling of mesoporous CMK-5 carbon studied by XRD: comparison between theoretical simulations and experimental results, Microporous Mesoporous Mater. 266 (2018) 24–31, https://doi.org/10.1016/j.micromeso.2018.02.035.

[49] B. Schwind, J.H. Smått, M. Tiemann, C. Weinberger, Modeling of gyroidal mesoporous CMK-8 and CMK-9 carbon nanostructures and their X-Ray diffraction patterns, Microporous Mesoporous Mater. 310 (2021), 110330, https://doi.org/10.1016/j.micromeso.2020.110330.

[50] V. Yelpo, V. Cornette, J.P. Toso, R.H. López, Characterization of nanostructured carbon CMK-3 by means of Monte Carlo simulations, Carbon 121 (2017) 106–113, https://doi.org/10.1016/j.carbon.2017.05.085.

[51] M.E. Casco, J. Silvestre-Albero, A.J. Ramírez-Cuesta, F. Rey, J.L. Jordá, A. Bansode, A. Urakawa, I. Peral, M. Martínez-Escandell, K. Kaneko, F. Rodríguez-Reinoso, Methane hydrate formation in confined nanospace can surpass nature, Nat. Commun. 6 (2015) 6432, https://doi.org/10.1038/ncomms7432.

[52] J. Górka, A. Zawislak, J. Choma, M. Jaroniec, Adsorption and structural properties of soft-templated mesoporous carbons obtained by carbonization at different temperatures and KOH activation, Appl. Surf. Sci. 256 (2010) 5187–5190, https://doi.org/10.1016/j.apsusc.2009.12.092.

[53] P.W. Xiao, L. Zhao, Z.Y. Sui, M.Y. Xu, B.H. Han, Direct synthesis of ordered mesoporous hydrothermal carbon materials via a modified soft-templating method, Microporous Mesoporous Mater. 253 (2017) 215–222, https://doi.org/10.1016/j.micromeso.2017.07.001.

[54] R. Janus, P. Natkański, M. Wądrzyk, M. Lewandowski, M. Michalik, P. Kuśtrowski, Deposition of poly(furfuryl alcohol) in mesoporous silica template controlled by

solvent polarity: A cornerstone of facile and versatile synthesis of high-quality CMK-type carbon replicas. Nanocasting of SBA-15, SBA-16, and KIT-6, Carbon 195 (2022) 292–307, https://doi.org/10.1016/j.carbon.2022.04.025.

[55] R. Janus, P. Natkański, M. Wądrzyk, M. Lewandowski, P. Łątka, P. Kuśtrowski, Effect of solvent polarity in formation of perfectly ordered CMK-3 and CMK-5 carbon replicas by precipitation polycondensation of furfuryl alcohol, Microporous Mesoporous Mater. 329 (2022), 111542, https://doi.org/10.1016/j.micromeso.2021.111542.

[56] M. Kaneda, T. Tsubakiyama, A. Carlsson, Y. Sakamoto, T. Ohsuna, O. Terasaki, S. H. Joo, R. Ryoo, Structural study of mesoporous MCM-48 and carbon networks synthesized in the spaces of MCM-48 by electron crystallography, J. Phys. Chem. B 106 (2002) 1256–1266, https://doi.org/10.1021/jp0131875.

[57] T.W. Kim, I.S. Park, R. Ryoo, A synthetic route to ordered mesoporous carbon materials with graphitic pore walls, Angew. Chem. Int. Ed. 42 (2003) 4375–4379, https://doi.org/10.1002/anie.200352224.

[58] J. Jagiello, C. Ania, J.B. Parra, C. Cook, Dual gas analysis of microporous carbons using 2D-NLDFT heterogeneous surface model and combined adsorption data of N_2 and CO_2, Carbon 91 (2015) 330–337, https://doi.org/10.1016/j.carbon.2015.05.004.

[59] J. Jagiello, J. Castro-Gutiérrez, R.L.S. Canevesi, A. Celzard, V. Fierro, Comprehensive analysis of hierarchical porous carbons using a dual-shape 2D-NLDFT model with an adjustable slit-cylinder pore shape boundary, ACS Appl. Mater. Interfaces 13 (2021) 49472–49481, https://doi.org/10.1021/acsami.1c13910.

[60] J. Jagiello, C.O. Ania, J.B. Parra, L. Jagiello, J.J. Pis, Using DFT analysis of adsorption data of multiple gases including H_2 for the comprehensive characterization of microporous carbons, Carbon 45 (2007) 1066–1071, https://doi.org/10.1016/j.carbon.2006.12.011.

[61] B. Boote, H. Subramanian, K.T. Ranjit, Rapid and facile synthesis of siliceous MCM-48 mesoporous materials, Chem. Commun. (2007) 4543–4545, https://doi.org/10.1039/b706633c.

[62] M.J. Kim, R. Ryoo, Synthesis and pore size control of cubic mesoporous silica SBA-1, Chem. Mater. 11 (1999) 487–491, https://doi.org/10.1021/cm980691m.

[63] R. Janus, M. Wądrzyk, M. Lewandowski, P. Natkański, P. Łątka, P. Kuśtrowski, Understanding pore structure of SBA-15 upon pseudomorphic transformation into MCM-41: non-direct investigation by carbon replication, J. Ind. Eng. Chem. 92 (2020) 131–144, https://doi.org/10.1016/j.jiec.2020.08.032.

[64] M. Jaroniec, M. Kruk, J.P. Olivier, Standard nitrogen adsorption data for characterization of nanoporous silicas, Langmuir 15 (1999) 5410–5413, https://doi.org/10.1021/la990136e.

[65] A. Silvestre-Albero, J. Silvestre-Albero, M. Martínez-Escandell, R. Futamura, T. Itoh, K. Kaneko, F. Rodríguez-Reinoso, Non-porous reference carbon for N_2 (77.4 K) and Ar (87.3 K) adsorption, Carbon 66 (2014) 699–704, https://doi.org/10.1016/j.carbon.2013.09.068.

[66] M. Thommes, K. Kaneko, A.V. Neimark, J.P. Olivier, F. Rodríguez-Reinoso, J. Rouquerol, K.S.W. Sing, Physisorption of gases, with special reference to the evaluation of surface area and pore size distribution (IUPAC Technical Report), Pure Appl. Chem. 87 (2015) 1051–1069, https://doi.org/10.1515/pac-2014-1117.

[67] W. Tanglumlert, T. Imae, T.J. White, S. Wongkasemjit, Structural aspects of SBA-1 cubic mesoporous silica synthesized via a sol-gel process using a silatrane precursor, J. Am. Ceram. Soc. 90 (2007) 3992–3997, https://doi.org/10.1111/j.1551-2916.2007.02076.x.

[68] P.I. Ravikovitch, A.V. Neimark, Density functional theory of adsorption in spherical cavities and pore size characterization of templated nanoporous silicas with cubic and three-dimensional hexagonal structures, Langmuir 18 (2002) 1550–1560, https://doi.org/10.1021/la0107594.

[69] A. Vinu, V. Murugesan, M. Hartmann, Pore size engineering and mechanical stability of the cubic mesoporous molecular sieve SBA-1, Chem. Mater. 15 (2003) 1385–1393, https://doi.org/10.1021/cm0213523.

[70] H.M. Kao, J. Da Wu, C.C. Cheng, A.S.T. Chiang, Direct synthesis of vinyl-functionalized cubic mesoporous silica SBA-1, Microporous Mesoporous Mater. 88 (2006) 319–328, https://doi.org/10.1016/j.micromeso.2005.10.002.

[71] M.C. Chao, H.P. Lin, D.S. Wang, C.Y. Mou, Synthesis of SBA-1 mesoporous silica crystals with tunable pore size using sodium silicate and alkyltrimethylammonium surfactants, Chem. Lett. 33 (2004) 374–375, https://doi.org/10.1246/cl.2004.374.

[72] S. Che, Y. Sakamoto, O. Terasaki, T. Tatsumi, Control of crystal morphology of SBA-1 mesoporous silica, Chem. Mater. 13 (2001) 2237–2239, https://doi.org/10.1021/cm010297f.

[73] M.C. Chao, D.S. Wang, H.P. Lin, C.Y. Mou, Control of single crystal morphology of SBA-1 mesoporous silica, J. Mater. Chem. 13 (2003) 2853–2854, https://doi.org/10.1039/b313028m.

[74] Y. Sakamoto, M. Kaneda, O. Terasaki, D.Y. Zhao, J.M. Kim, G. Stucky, H.J. Shin, R. Ryoo, Direct imaging of the pores and cages of three-dimensional mesoporous materials, Nature 408 (2000) 449–453, https://doi.org/10.1038/35044040.

[75] K. Schumacher, P.I. Ravikovitch, A. Du Chesne, A.V. Neimark, K.K. Unger, Characterization of MCM-48 materials, Langmuir 16 (2000) 4648–4654, https://doi.org/10.1021/la991595i.

[76] J.M. Kim, S.K. Kim, R. Ryoo, Synthesis of MCM-48 single crystals, Chem. Commun. 1 (1998) 259–260, https://doi.org/10.1039/a707677k.

[77] A. Galarneau, M.F. Driole, C. Petitto, B. Chiche, B. Bonelli, M. Armandi, B. Onida, E. Garrone, F. Di Renzo, F. Fajula, Effect of post-synthesis treatment on the stability and surface properties of MCM-48 silica, Microporous Mesoporous Mater. 83 (2005) 172–180, https://doi.org/10.1016/j.micromeso.2005.03.020.

[78] T. Da Silveira, C.M. Awano, D.A. Donatti, F.S. De Vicente, D.R. Vollet, About the thermal stability and pore elimination in the ordered hexagonal mesoporous silica SBA-15, Microporous Mesoporous Mater. 190 (2014) 227–233, https://doi.org/10.1016/j.micromeso.2014.02.023.

[79] K.P. Gierszal, M. Jaroniec, T.W. Kim, J. Kim, R. Ryoo, High temperature treatment of ordered mesoporous carbons prepared by using various carbon precursors and ordered mesoporous silica templates, New J. Chem. 32 (2008) 981–993, https://doi.org/10.1039/b716735k.

[80] A. Galarneau, D. Mehlhorn, F. Guenneau, B. Coasne, F. Villemot, D. Minoux, C. Aquino, J.P. Dath, Specific surface area determination for microporous/mesoporous materials: the case of mesoporous FAU-Y zeolites, Langmuir 34 (2018) 14134–14142, https://doi.org/10.1021/acs.langmuir.8b02144.